RESEARCH ARTICLE

NANO · MICRO small
www.small-journal.com

Plasma-Enhanced Grain Growth and Non-Radiative Recombination Mitigation in $CsSnBr_3$ Perovskite Films for High-Performance, Lead-Free Photodetectors

Zewen Lin, Zhenxu Lin, Haixia Wu, Rui Huang, Jie Song, Kaitao Chen, Li Xia, Yi Zhang, Huihong Lin, Hongliang Li, Dejian Hou, Yanqing Guo, and Paul K. Chu**

Tin-based halide perovskites represent a highly promising and eco-friendly alternative to lead-based materials with significant potential for optoelectronic applications. However, their advancement is hampered by challenges such as poor film crystallinity and unintended self-doping. Herein, this work reports the fabrication of high-quality $CsSnBr_3$ perovskite films by plasma-assisted chemical vapor deposition (PACVD), which improves the film quality. The precise control of the ammonia plasma not only promotes grain growth and reduces grain boundaries, but also eliminates defect states in the film, mitigates oxidation of Sn^{2+}, suppresses sub-bandgap absorption, and reduces non-radiative recombination. Consequently, the photodetectors deliver exceptional performance, including a responsivity of 11.2 A W^{-1}, a detectivity of 2.5×10^{11} Jones, and an ultrafast response time of 1/3.3 ms. Notably, certain key metrics, including detectivity (D*) and response time, significantly surpass those of all previously reported photoconductor-type Sn-based perovskite photodetectors. The results offer not only a novel strategy for enhancing the quality and optoelectronic performance of $CsSnBr_3$ films but also a scalable platform for the development of high-performance, lead-free perovskite materials and devices. The new knowledge opens new possibilities for the design and fabrication of sustainable materials for advanced optoelectronic applications.

1. Introduction

Metal halide perovskites are very promising in applications such as photovoltaics, light-emitting devices, and photodetectors due to their remarkable optoelectronic properties.[1–5] Notably, lead-free metal halide perovskites have garnered considerable interest because of their low toxicity, making them a desirable alternative for sustainable technological development.[6–8] In this context, tin-based halide perovskites have emerged as the most viable and less toxic alternative to lead-based perovskites. This is largely because the ionic radius of Sn^{2+} (135 pm) is similar to that of Pb^{2+} (149 pm) in addition to the similar electronic configuration (ns^2np^2). These factors endow tin-based perovskites with optoelectronic properties comparable to those of the lead-based counterparts, for example, high charge carrier mobility, extended carrier lifetime, and strong light absorption, thereby making them promising for solar cells and various optoelectronic applications.[9–13] However, tin-based halide perovskite devices suffer from some drawbacks, particularly the poor quality of Sn-based perovskite films, on accountof the susceptibility of Sn^{2+} to oxidation and uncontrolled crystallization.[14,15] Sn^{2+} is easily oxidized to Sn^{4+}, leading to the formation of Sn vacancies and p-type characteristics, which trigger undesirable self-doping effects and produce large dark currents in the films.[16,17] Moreover, the accumulation of Sn vacancies can create deep-level defects, such as antisite defects and substitutional defects, both of which are linked to significant nonradiative recombination.[18] Furthermore, the uncontrolled crystallization process, driven by Sn^{2+}'s high Lewis acidity, typically results in small grain sizes, numerous pinholes, and high trap state densities in the films, further degrading device performance.[19,20] To overcome these hurdles, several strategies have been proposed, including solvent engineering,[21–23] additive engineering,[24–27] cation engineering,[28] and advanced film-forming techniques.[29,30] For example, ascorbic acid and SnF_2 have been utilized as effective reducing agents to stabilize the black phase of α-$CsSnI_3$ to enable precise control of nucleation and growth and to inhibit Sn oxidation and minimize Sn vacancy formation.[26] Similarly, Liu et al. have shown that thiophene-2-carbohydrazide significantly increases the grain size from 477.69 to 756.09 nm, while effectively suppressing Sn^{2+} oxidation, giving rise to a notable reduction in the dark current to

Z. Lin, Z. Lin, H. Wu, R. Huang, J. Song, K. Chen, L. Xia, Y. Zhang, H. Lin, H. Li, D. Hou, Y. Guo
School of Materials Science and Engineering
Hanshan Normal University
Chaozhou, Guangdong 521041, P. R. China
E-mail: rhuang@hstc.edu.cn
P. K. Chu
Department of Physics
Department of Materials Science and Engineering
and Department of Biomedical Engineering
City University of Hong Kong
Tat Chee Avenue, Kowloon, Hong Kong 999077, China
E-mail: paul.chu@cityu.edu.hk

The ORCID identification number(s) for the author(s) of this article can be found under https://doi.org/10.1002/smll.202411086

DOI: 10.1002/smll.202411086

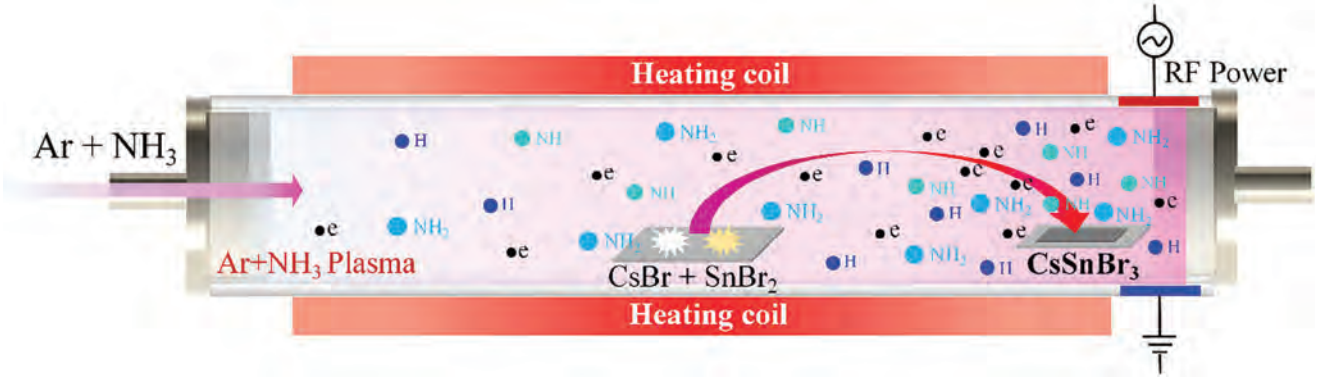

Figure 1. Schematic diagram showing the plasma-assisted chemical vapor deposition for the synthesis of high-quality $CsSnBr_3$ films.

1.5×10^{-8} mA cm^{-2} at a bias of-0.07 V, which is three times lower than that of the untreated films.[27] Liu et al. have optimized the chemical vapor deposition (CVD) process to produce $CsSnBr_3$ films with fewer grain boundaries and pinholes and prepared a two-terminal photodetector with a high responsivity of 9.2 A W^{-1}, detectivity of 5.8×10^7, and a small dark current of 300 nA.[30] However, despite these recent advancements, the properties of tin-based perovskite devices are still inferior to those of their lead-based counterparts, and hence, further research and refinement are needed to unlock their full potential.[31]

Plasma-enhanced chemical vapor deposition (PECVD) is widely used in film deposition and is, in fact, one of the industrial workhorses for producing high-quality films. It is well known that activation by the glow discharge plasma enhances the reactivity of the materials, accelerates surface reactions, and promotes the development of dense and uniform films with superior properties. However, despite these advantages, glow discharge plasma has not been demonstrated to improve the quality of perovskite films. In fact, its application has largely been confined to surface modification of halide perovskite films to improve device performance and stability.[32–34] The primary challenge lies in the absence of suitable precursors for the PECVD-based synthesis of perovskite films. Therefore, while glow discharge plasma generates highly reactive intermediates that can foster high-quality film growth, its precise role in halide perovskite film formation remains unclear, particularly $CsSnBr_3$.

In this work, in order to address these uncertainties and assess the potential of plasma-enhanced techniques for high-quality $CsSnBr_3$ film growth, a plasma-assisted chemical vapor deposition (PACVD) protocol is designed and demonstrated, as shown in **Figure 1**. This approach integrates the glow discharge plasma with the traditional quartz tube CVD process. Specifically, CsBr and $SnBr_2$ powders are evaporated in CVD to serve as the precursors for the growth of $CsSnBr_3$ films. Concurrently, an Ar and/or Ar+NH_3 plasma, generated by a 13.56 MHz RF source, is introduced to investigate its effects on the formation of high-quality $CsSnBr_3$ films. Our findings reveal that the ammonia plasma-assisted process not only promotes grain growth and reduces grain boundaries, but also eliminates defect states in the film, mitigates the oxidation of Sn^{2+}, and suppresses sub-bandgap absorption. This, in turn, minimizes non-radiative recombination centers. Consequently, the photodetectors fabricated with these films have outstanding properties.

2. Results and Discussion

Figure 2a–e depicts the morphologies of the samples deposited using different plasma power settings. When the power is increased from 0 to 10 W, the primary grain size of the sample markedly expands from ≈1.5 to ≈4.0 µm (Figure S1, Supporting Information), while the grain density decreases, indicating a reduction in grain boundaries. However, at 30 W, the grain size diminishes together with a corresponding increase in the grain density. Energy-dispersive X-ray spectroscopy (EDS) (Figure S2a–e, Supporting Information) confirms homogeneous Cs, Sn, and Br distributions across the films and a 1:1:3 atomic ratio consistent with $CsSnBr_3$. The film deposition rate increases gradually with increasing RF power (Figure S3, Supporting Information), and the rate at 30 W exceeds that of the sample deposited without plasma by over 30%. X-ray diffraction (XRD) verifies the sample quality (Figure 2f), revealing a polycrystalline cubic perovskite structure (JCPDS No.22-0199) with the Pm3 m symmetry.[30] The diffraction peaks at 21.6°, 26.6°, 30.8°, 34.6°, 38.0°, and 44.1° correspond to the (110), (111), (200), (210), (211), and (220) planes of $CsSnBr_3$. These results suggest that the Ar plasma with the proper power enhances grain growth. This improvement arises from the Ar plasma's ability to promote the decomposition of $CsBr_2$ and $SnBr_2$, thereby intensifying chemical reactions of these highly reactive precursors on the substrate surface and facilitating grain growth. However, as illustrated in Figure S3, Supporting Information, an excessive power level accelerates the growth rate and hinders grain growth by restricting the time available for surface atoms to diffuse and reorganize. This phenomenon accounts for the reduction in grain size as the power is increased from 10 W to 30 W.

According to Figure S4, Supporting Information, all the $CsSnBr_3$ films show a same sharp absorption edge at ≈652 nm. The bandgap of $CsSnBr_3$ is determined to be 1.8 eV according to the Tauc plot of the absorption spectrum (inset of Figure S3, Supporting Information).[35] All the films exhibit an emission peak near 685 nm characteristic of $CsSnBr_3$ (**Figure** 3a). Interestingly, the $CsSnBr_3$ films prepared with the Ar plasma show markedly enhanced steady-state photoluminescence (PL) intensity and extended PL lifetime compared to films without the plasma treatment (Figure 3a,b). Specifically, the PL intensity increases by more than two times at P = 10 W, and the average PL lifetime increases from ≈0.3 to 1.3 ns (Figure 3b).[36] The

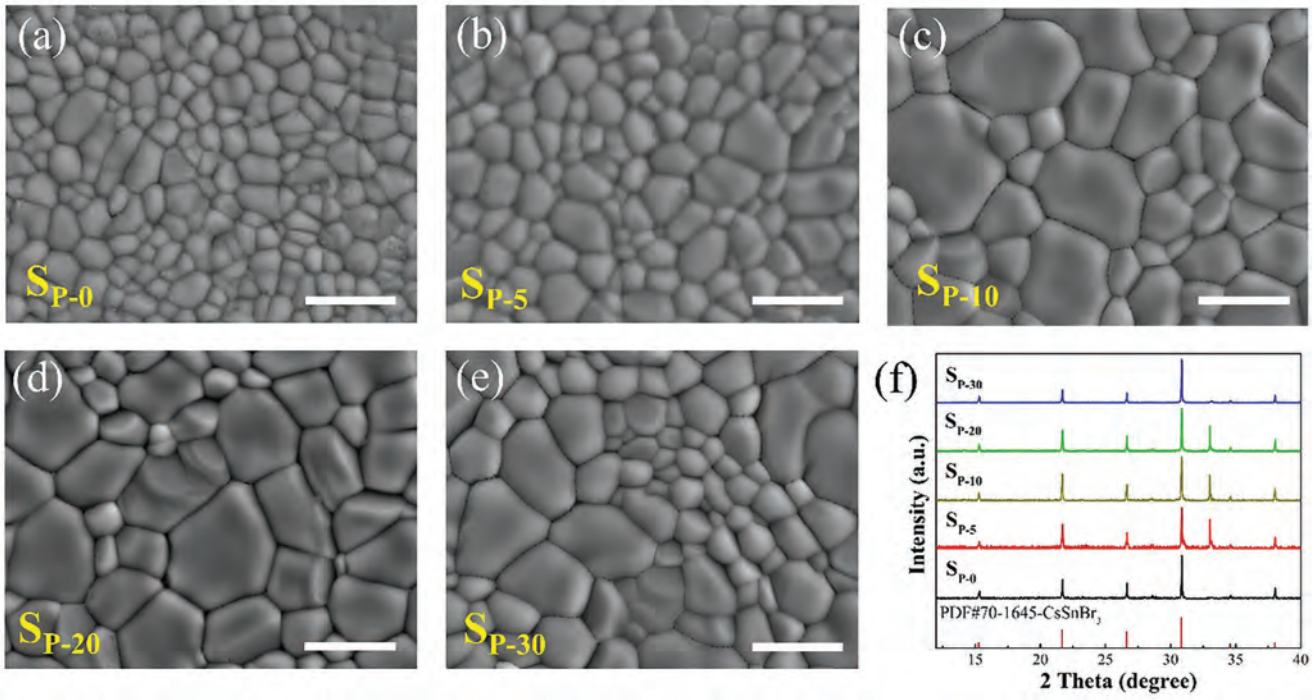

Figure 2. Scanning electron microscope (SEM) images of $CsSnBr_3$ films prepared using various RF power settings: a) No RF power, b) 5 W, c) 10 W, d) 20 W, and e) 30 W; All scale bars are 5 µm. (f) XRD patterns of $CsSnBr_3$ films prepared with different RF power settings.

correlation between the PL intensity and lifetime with power aligns with the grain size variation (Figure 2a–e), suggesting that the improved PL properties are attributed to reduced grain boundaries due to increased grain size, thereby effectively minimizing non-radiative recombination centers in the film.

In order to passivate the non-radiative recombination centers in the films, an NH_3 plasma treatment is implemented in addition to the Ar plasma. Notably, SEM analysis reveals a pronounced effect of ammonia plasma on grain size within the film. When the ammonia flow rate is raised from 5to 15 sccm, the main grain size expands remarkably from ≈6 to ≈10 µm. Evidently, ammonia plasma assistance during growth results in a grain size more than six times larger than that observed in films grown without plasma assistance (**Figure 4**). XRD is performed to investigate potential changes in crystal structure after the NH_3 plasma treatment. All the $CsSnBr_3$ films have the Pm3 m cubic phase, regardless of the NH_3 plasma treatment. There are no observable peak shifts (Figure S5, Supporting Information), indicating that the lattice constant does not change after the NH_3 plasma treatment. As shown in **Figure 5a**, the samples exhibit nearly the same sharp absorption edges, corresponding to an optical bandgap of 1.8 eV. However, in the sub-bandgap region between 1.0 and 1.7 eV, the absorption coefficients of the films deposited with the NH_3 plasma are lower than those of the films

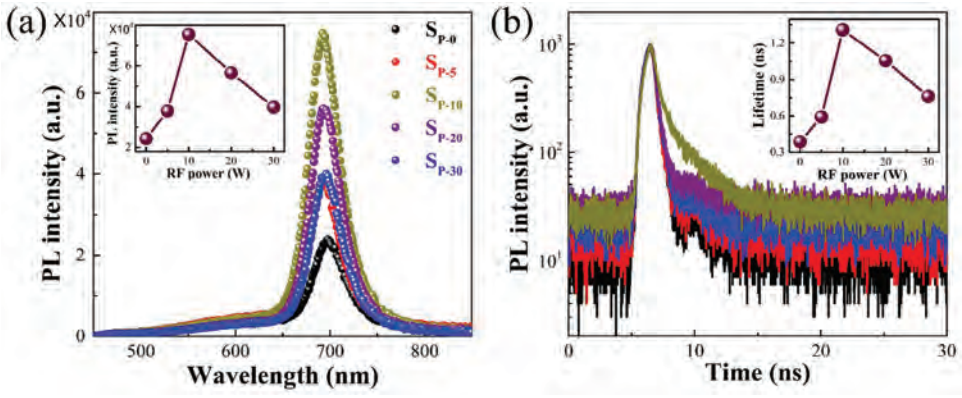

Figure 3. a) PL spectra of $CsSnBr_3$ films deposited at different RF power levels using the 340 nm Xe lamp. The inset shows the PL intensity as a function of RF power. b) TRPL spectra of $CsSnBr_3$ films deposited at various RF power settings, monitored at 695 nm with an excitation wavelength of 375 nm, generated by 70 ps laser pulses. The inset shows the PL lifetime as a function of RF power. The intensity-weighted average PL lifetimes were determined as outlined in.[36]

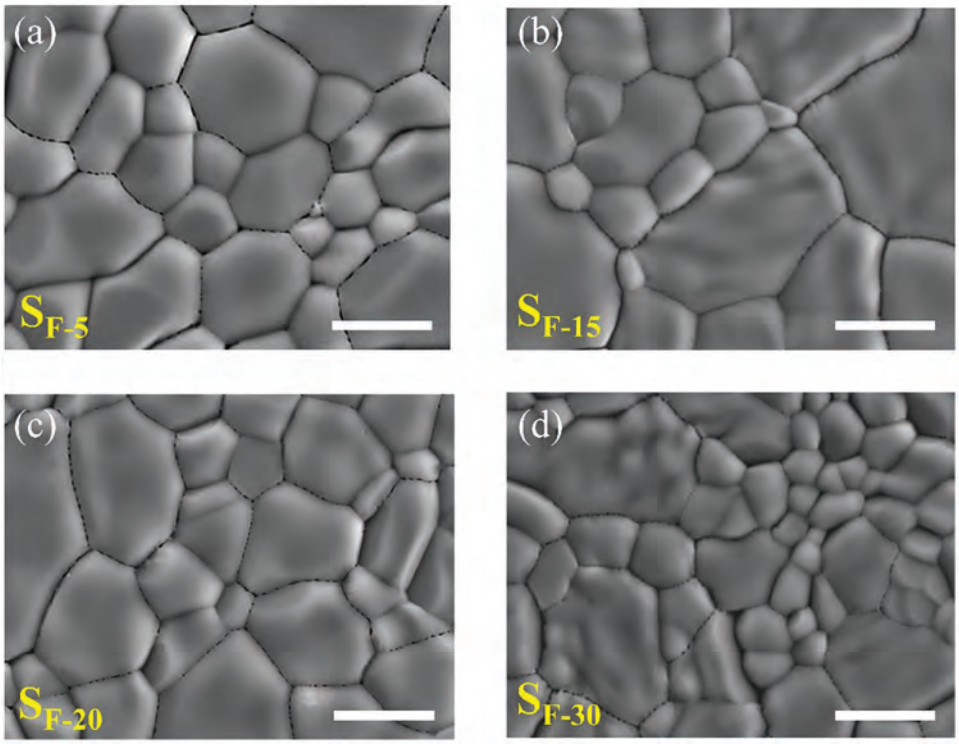

Figure 4. SEM images of the $CsSnBr_3$ films prepared at different NH_3 flow rates: a) 5 sccm, b) 15 sccm, c) 20 sccm, and d) 30 sccm. The scale bars are 5 µm.

without plasma treatment. The reduced absorption is associated with less deep-level electron transitions, suggesting a reduction in the density of deep defect states. Notably, the sample prepared with 15 sccm NH_3 exhibits the smallest absorption coefficient, implying minimal deep defect states. Further increasing the NH_3 flow rate to 30 sccm increases the absorption coefficient, suggesting increased disorder and additional defect states. The luminescence intensity increases significantly after the NH_3 plasma treatment (Figure 5b). Specifically, the PL intensity more than doubles for an NH_3 flow rate of 15 sccm, while the average PL lifetime increases from ≈1.3 to 2.3 ns as the flow rate is increased from 0 to 15 sccm (Figure 5c). These results confirm the substantial reduction in the number of non-radiative recombination centers in the films. Conversely, if the NH_3 flow rate is increased from 15 sccm to 30 sccm, the luminescence intensity and PL lifetime decrease due to more defect states caused by the excessive NH_3 plasma treatment as discussed earlier.

Figure 5d presents the X-ray photoelectron spectroscopy (XPS) spectra of the samples prepared at different NH_3 flow rates. As the NH_3 flow rate is increased from 0 to 15 sccm, the Sn $3d_{5/2}$ peak at ≈487 eV shifts to lower binding energies compared to the pristine $CsSnBr_3$, indicating suppressed Sn^{2+} oxidation to Sn^{4+}, because Sn^{2+} has a smaller binding energy than Sn^{4+}.[37] The chemical bonding in the $CsSnBr_3$ films is further analyzed by deconvoluting the Sn $3d_{5/2}$ XPS peaks, revealing two components at 486.6 eV and 487.4 eV corresponding to Sn^{2+} and Sn^{4+}, respectively.[37] In the pristine $CsSnBr_3$ film, the Sn^{4+} peak is dominant over the Sn^{2+} peak. However, with increasing NH_3 flow rates from 0 to 15 sccm, the Sn^{2+}/Sn^{4+} ratio increases from 0.86 to 1.17, indicating that the NH_3 plasma suppresses the oxidation of Sn^{2+} and mitigates the formation of Sn^{4+}, which would otherwise contribute to defect states and non-radiative recombination. As shown in Figure S6, Supporting Information, it is suggested that during film deposition, the NH_3 plasma generates active species such as H, NH, and NH_2[32] to passivate surface defects, typically sites responsible for Sn^{2+} oxidation. By decreasing these oxidation-prone sites, the NH_3 plasma mitigates Sn^{2+} oxidation. Meanwhile, the active species form coordination bonds with undercoordinated Sn to passivate defects.[38] Recent investigations have shown that NH and NH_2 functional groups influence the coordination environment of the precursor solution. These functional groups interact with the ingredients in the solution to regulate crystal nucleation and growth, thus promoting the formation of high-quality perovskite films.[39–41] For instance, NH_2 functional groups can coordinate with Sn^{2+}/Pb^{2+} to slow crystal growth and enhance the grain size in the mixed Sn-Pb perovskites.[40] In this study, the nitrogen atom in the NH or NH_2 functional group possesses lone-pair electrons, thus acting as a Lewis base and facilitating the coordination with Sn^{2+}, which serves as a Lewis acid. The coordination alters the local chemical environment surrounding the metal ions and temporarily "passivates" the metal ions, thereby reducing their reactivity and impeding crystallization. Consequently, the growth of larger $CsSnBr_3$ grains is enhanced, leading to a reduction in grain boundaries and better film quality. This hypothesis is corroborated by SEM observations, which clearly show improved grain morphology with increasing NH_3 flow rates. Figure S7a, Supporting Information shows that the PL intensity of the sample prepared

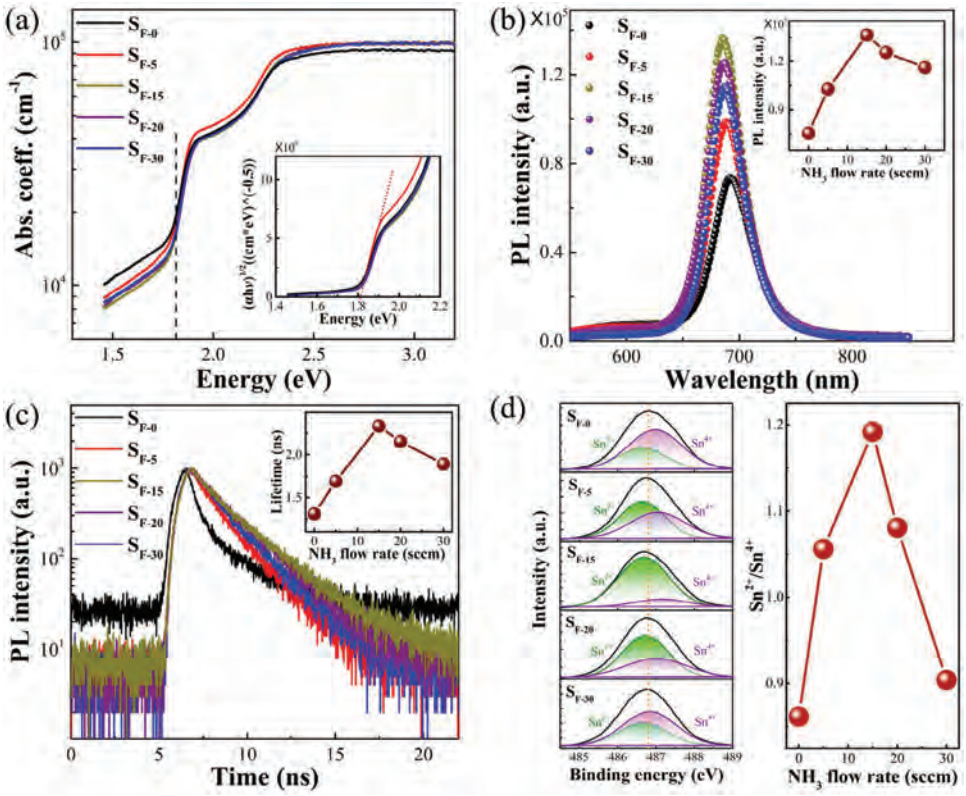

Figure 5. a) Optical absorption spectra of $CsSnBr_3$ films prepared at different NH_3 flow rates. The inset shows the Tauc plots of the $CsSnBr_3$ films derived from the absorption spectra. b) PL spectra of the $CsSnBr_3$ films deposited at various NH_3 flow rates excited by the 340 nm Xe lamp. The inset shows the PL intensity as a function of NH_3 flow rates. c) TRPL spectra of the $CsSnBr_3$ films prepared at different NH_3 flow rates monitored at 695 nm. The inset shows the PL lifetime as a function of NH_3 flow rates. d) Deconvolution of the XPS Sn 3*d* spectra of the $CsSnBr_3$ films deposited at different NH_3 flow rates. The green and purple spectra correspond to Sn^{4+} and Sn^{2+}, respectively.

without NH_3 plasma decreases rapidly by 90% after just 1 day and is nearly completely quenched after 13 days. In contrast, the sample prepared with the NH_3 plasma treatment exhibits significantly better stability, with a reduction in PL intensity of only 15% after 1 day (Figure S7b, Supporting Information). After 5 days, the PL intensity decreases by 50%, and it remains stable thereafter, maintaining a constant intensity for up to 15 days. These results demonstrate that the chemical stability of $CsSnBr_3$ films can be significantly enhanced by NH_3 plasma-assisted growth. It is clear that the precise control of the ammonia plasma not only eliminates defect states in the film and mitigates the oxidation of Sn^{2+}, but also facilitates grain growth and improves the optoelectronic properties and stability of $CsSnBr_3$ films.

To demonstrate the potential application of $CsSnBr_3$ films to optoelectronic devices, planar-type photodetectors with a metal-semiconductor-metal structure are fabricated. An interdigital Au electrode with a spacing of 50 µm is deposited by magnetron sputtering with a mask. The structure and optical image of the photodetector are depicted in **Figure 6**a. The effective area of the device is ≈0.68 mm^2. Figure 6b and Figure S8, Supporting Information present the current-voltage (I-V) characteristics of devices A, B, and C, both in darkness and upon illumination with 625 nm light at power densities ranging from 0 to 0.8 mW cm^{-2}. Device C, with a dark current of only 7.1 nA at 1 V, shows a substantially smaller dark current compared to device A (≈200 nA). Moreover, at a light power density of 0.8 mW cm^{-2}, the photocurrent reaches 2653 nA, which is significantly bigger than those of devices A (≈990 nA) and B (≈1500 nA). The reduced dark current and enhanced photocurrent observed from device C can be attributed to the larger grain size and lower defect state density of the $CsSnBr_3$ film, resulting in enhanced photoelectric currents in the visible spectrum (Figures S8 and S9, Supporting Information). This also improves the ON/OFF current ratio of the photodetector. It is evident that the photocurrent increases with increasing light power density (Figure 6c). However, there is a notable difference in their linear dynamic range (LDR), with device C exhibiting the widest LDR (68 dB).

To assess the performance of the photodetector, the photoresponsivity (R) is calculated by the formula: $R = (I_p - I_d)/(P \cdot S)$, where I_p is the photocurrent, I_d is the dark current, P is the incident light intensity, and S is the effective illuminated area.[42] The calculated photoresponsivity as a function of incident light power under different light illuminations is presented in Figure 6d and Figure S10c,d, Supporting Information. Under illumination with a 625 nm laser at an intensity of 0.8 mW cm^{-2}, Device C achieves the highest responsivity of 11.2 A W^{-1}, significantly surpassing the other two devices. The specific detectivity (D*), an important figure-of-merit characterizing the minimum detectable signal, is evaluated by the formula: $D^* = R \cdot S^{1/2}/(2e \cdot I_{dark})^{1/2}$, where e is the electronic charge.[43] Figure 6e

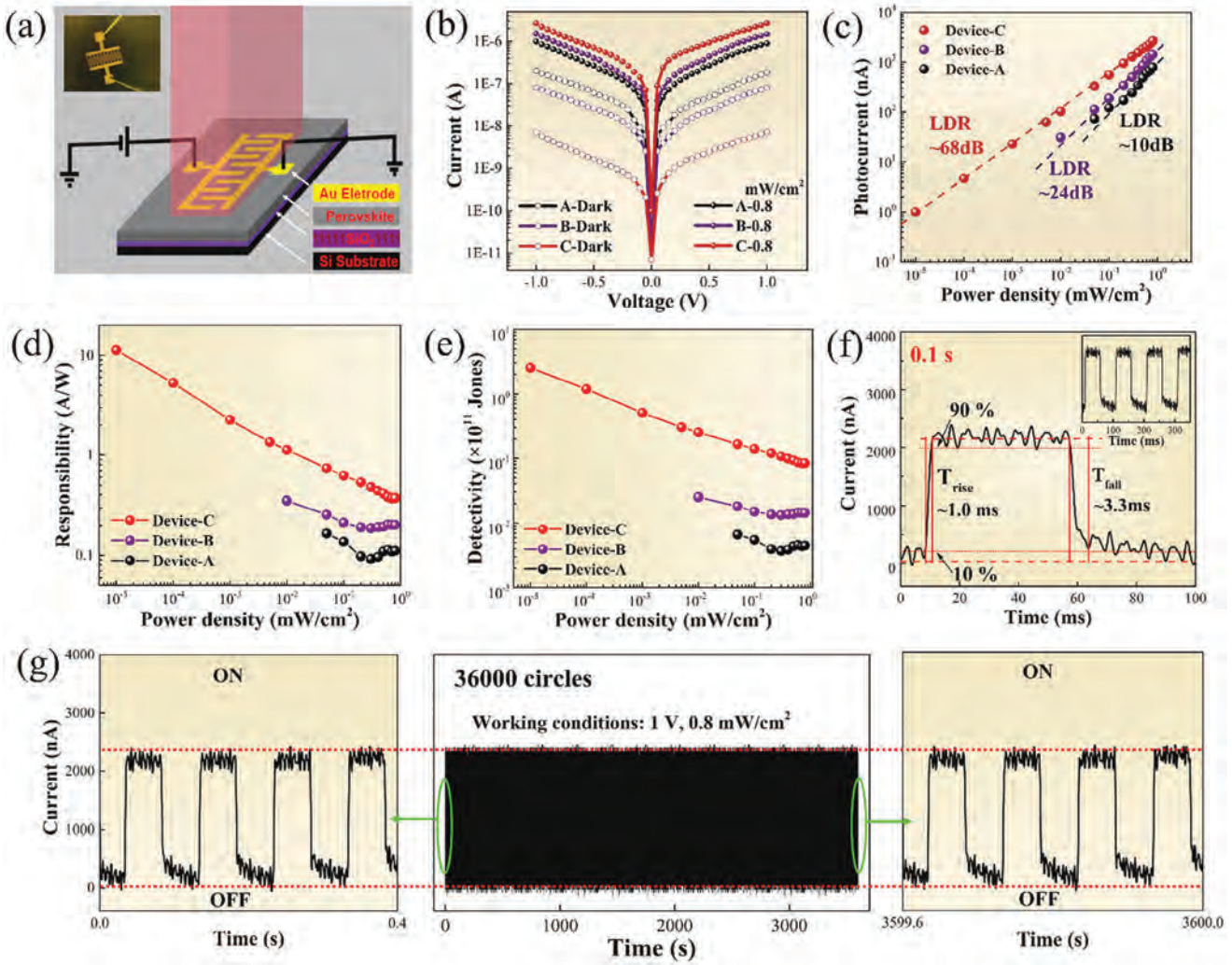

Figure 6. a) Schematic structure and optical image of the photodetector. b) Typical logarithmic I–V curves of the photodetectors composed of $CsSnBr_3$ films prepared without RF power (device A), with an Ar RF power of 10 W (device B), and with an NH_3 flow rate of 15 sccm and RF power of 10 W (device C), measured in the dark and under illumination with 625 nm laser with an intensity of 0.8 mW cm^{-2}. c) Dependence of photocurrents on illumination power densities for devices A, B, and C. d) Responsivity (R) and e) Specific detectivity (D*) of different devices (A, B, C) under illumination with a 625 nm laser with an intensity of 0.8 mW cm^{-2}. f) Time-response curves, including rise and decay times of device C upon 625 nm laser illumination. g) Current-time (I–t) curves of device C at a bias voltage of 1 V and illuminated by 0.8 mW cm^{-2}.

and Figure S10e,f, Supporting Information show the relationship between D* and incident irradiance power under various light illuminations. Devices A, B, and C exhibit maximum D* values of 0.7×10^9, 1.1×10^{10}, and 2.5×10^{11} Jones, respectively, when illuminated with a 625 nm laser. Device C also shows a faster response time, as illustrated in Figure 6f. The rise time (T_{rise}) and fall time (T_{fall}) are defined as those required for the photocurrents to change from 10% to 90% and from 90% to 10% of the stable value during light switching, respectively.[44] The T_{rise} and T_{fall} values of device C are calculated to be 1.0 and 3.3 ms, respectively, which are significantly shorter than those of the other two devices (Figure S11, Supporting Information). Notably, the response time of the photodetector comprising the $CsSnBr_3$ perovskite film deposited by Ar + NH_3 plasma-assisted CVD is considerably shorter than those of the photodetector based on CVD $CsSnBr_3$ without plasma assistance.[30,45] Furthermore, device C exhibits uniform and stable photo-response for 3600 s under ambient conditions (Figure 6g), reflecting significantly better stability than the other two devices (Figure S12, Supporting Information). Table S1, Supporting Information summarizes the properties of recently reported lead-free halide perovskite photodetectors with similar MSM structures. It is evident that our photodetector, composed of $CsSnBr_3$ films deposited with the Ar + NH_3 plasma, exhibits excellent stability, superior responsivity, fastest response time, as well as highest detectivity. This highlights the potential of the Ar + NH_3 plasma-assisted process in enhancing the performance of $CsSnBr_3$ perovskite-based photodetectors.

3. Conclusion

High-quality $CsSnBr_3$ perovskite films are prepared by an optimized PACVD protocol to address the poor crystallinity and

unintended self-doping. The precise control of the ammonia plasma not only eliminates defect states in the film and mitigates the oxidation of Sn^{2+}, but also facilitates grain growth and improves the optoelectronic properties and stability of $CsSnBr_3$ films. Consequently, the photodetectors constructed with the films have exceptional characteristics, including impressive detectivity and ultrafast response time, which are better than those of previously reported photoconductor-type Sn-based perovskite photodetectors. These results reveal a simple, cost-effective, and scalable method to enhance the quality and properties of lead-free $CsSnBr_3$ perovskite films and the new information enriches our knowledge and provides insights into the advancement and development of environmentally friendly, high-performance optoelectronic devices. This strategy also provides guidance and opens new avenues for the exploration of sustainable perovskite materials for various advanced optoelectronic applications.

4. Experimental Section

Materials: Cesium bromide (CsBr, 99.9%) and stannous bromide ($SnBr_2$, 99.9%) were purchased from Aladdin Corp. (China) and used as received without further purification.

Preparation of $CsSnBr_3$ Films: The $CsSnBr_3$ films were deposited by a simple, plasma-assisted, one-step chemical vapor deposition technique in a quartz tube furnace, in which $SnBr_2$ (0.05 g) and CsBr (0.05 g) powders were placed in the high-temperature zone, while the SOI substrate was positioned in the lower temperature region. The precursor powders, consisting of cesium bromide and tin bromide with a 3:4 molar ratio, were loaded onto a quartz crucible and placed in the center of the furnace. A base pressure of 0.5 Pa was set up in the quartz tube, and then argon (40 sccm, 99.9999% purity) was introduced to maintain a working pressure of 85 Pa. The materials in the high-temperature zone were heated at a rate of 20 °C min^{-1} to 630 °C, at which point the glow discharge plasma was ignited with RF power ranging from 5 to 40 W. Deposition proceeded for 15 min, and the $CsSnBr_3$ film was obtained after cooling naturally to room temperature. Samples prepared under different Ar RF power levels were labeled $S_{P\text{-}X}$, where X = 0, 5, 10, 20, and 30 corresponded to the applied Ar RF power. The N-doped $CsSnBr_3$ films were prepared by a similar protocol except using NH_3 (99.9999% purity) in lieu of argon. The NH_3 flow rate was adjusted between 5 and 30 sccm while maintaining the same conditions as described above. Samples produced with varying NH_3 flow rates were denoted as $S_{F\text{-}X}$, where X = 5, 15, 20, and 30 represented the NH_3 flow rate used during deposition.

Device Fabrication and Photoelectrical Properties: The planar-type photodetectors with a metal-semiconductor-metal structure were fabricated by depositing an interdigital Au electrode with a spacing of 50 µm by magnetron sputtering using a custom-designed mask. The electrical and photodetection properties of the devices were evaluated at room temperature using a Keithley 6517B electrometer in conjunction with a probe station. The photocurrent measurements were conducted with lasers of 280, 365, 450, 550, 625, and 730 nm. The response time was determined on the Rigol MSO7014 oscilloscope combined with a pulsed 625 nm laser.

Characterization: The surface morphology of the films was examined on the Hitachi SU5000 SEM equipped with a Bruker EDS QUANTAX system forEDS mapping. The crystal structure and crystallinity of the films were assessed byXRD using the X'pertPro Panalytical diffractometer. PL and time-resolved photoluminescence measurements were performed on the Edinburgh Instruments FLS1000 spectrometer, and the UV-vis absorption spectra were acquired on the Shimadzu UV-3600 spectrophotometer.

Supporting Information

Supporting Information is available from the Wiley Online Library or from the author.

Acknowledgements

Z.L., Z.L. and H.W. are contributed equally to this work. This work was supported by the Guangdong Basic and Applied Basic Research Foundation, Research Projects of the Department of Education of Guangdong Province (2021ZDJS039, 2024ZDZX1026), and City University of Hong Kong Donation Research Grants (9220061 and DON-RMG 9229021).

Conflict of Interest

The authors declare no conflict of interest.

Data Availability Statement

The data that support the findings of this study are available from the corresponding author upon reasonable request.

Keywords

chemical vapor deposition, $CsSnBr_3$ films, photoconductors, photodetectors, plasma

Received: November 20, 2024
Revised: December 17, 2024
Published online: January 5, 2025

[1] M. Liu, Q. Wan, H. Wang, F. Carulli, X. Sun, W. Zheng, L. Kong, Q. Zhang, C. Zhang, Q. Zhang, S. Brovelli, L. Li, *Nat. Photonics* **2021**, *15*, 379.
[2] J. S. Kim, J. M. Heo, G. S. Park, S. J. Woo, C. Cho, H. J. Yun, D. H. Kim, J. Park, S. C. Lee, S. H. Park, E. Yoon, N. C. Greenham, T. W. Lee, *Nature* **2022**, *611*, 688.
[3] Y. Sun, L. Ge, L. Dai, C. Cho, J. F. Orri, K. Ji, S. J. Zelewski, Y. Liu, A. J. Mirabelli, Y. Zhang, J. Y. Huang, Y. Wang, K. Gong, M. C. Lai, L. Zhang, D. Yang, J. Lin, E. M. Tennyson, C. Ducati, S. D. Stranks, L. S. Cui, N. C. Greenham, *Nature* **2023**, *615*, 830.
[4] Z. Han, W. Fu, Y. Zou, Y. Gu, J. Liu, B. Huang, D. Yu, F. Cao, X. Li, X. Xu, H. Zeng, *Adv. Mater.* **2021**, *33*, 2003852.
[5] G. Tong, H. Li, D. Li, Z. Zhu, E. Xu, G. Li, L. Yu, J. Xu, Y. Jiang, *Small* **2018**, *14*, 1702523.
[6] B. Su, J. Jin, K. Han, Z. Xia, *Adv. Funct. Mater.* **2023**, *33*, 2210735.
[7] T. H. Chowdhury, Y. Reo, A. R. B. M. Yusoff, Y. Y. Noh, *Adv. Sci.* **2022**, *9*, 2203749.
[8] J. Luo, X. Wang, S. Li, J. Liu, Y. Guo, G. Niu, L. Yao, Y. Fu, L. Gao, Q. Dong, C. Zhao, M. Leng, F. Ma, W. Liang, L. Wang, S. Jin, J. Han, L. Zhang, J. Etheridge, J. Wang, Y. Yan, E. H. Sargent, J. Tang, *Nature* **2018**, *563*, 541.
[9] W. Jang, K. Kim, B. G. Kim, J.-S. Nam, I. Jeon, D. H. Wang, *Adv. Funct. Mater.* **2022**, *32*, 2207713.
[10] L. Wang, Q. Miao, D. Wang, M. Chen, H. Bi, J. Liu, A. K. Baranwal, G. Kapil, Y. Sanehira, T. Kitamura, T. Ma, Z. Zhang, Q. Shen, S. Hayase, *Angew. Chem., Int. Ed.* **2023**, *62*, 202307228.
[11] W. F. Yang, F. Igbari, Y. H. Lou, Z. K. Wang, L. S. Liao, *Adv. Energy Mater.* **2020**, *10*, 1902584.
[12] G. Nasti, A. Abate, *Adv. Energy Mater.* **2020**, *10*, 1902467.
[13] A. M. Najarian, M. Vafaie, A. Johnston, T. Zhu, M. Wei, M. I. Saidaminov, Y. Hou, S. Hoogland, F. P. G. de Arquer, E. H. Sargent, *Nat. Electron.* **2022**, *5*, 511.
[14] J. Liu, H. Yao, S. Wang, C. Wu, L. Ding, F. Hao, *Adv. Energy Mater.* **2023**, *13*, 2300696.

[15] H. Dong, C. Ran, W. Gao, N. Sun, X. Liu, Y. Xia, Y. Chen, W. Huang, *Adv. Energy Mater.* **2022**, *12*, 2102213.
[16] Y. Zhang, Y. Ma, Y. Wang, X. Zhang, C. Zuo, L. Shen, L. Ding, *Adv. Mater.* **2021**, *33*, 2006691.
[17] D. Ricciarelli, D. Meggiolaro, F. Ambrosio, F. De Angelis, *ACS Energy Lett.* **2020**, *5*, 2787.
[18] B. Chen, P. N. Rudd, S. Yang, Y. Yuan, J. Huang, *Chem. Soc. Rev.* **2019**, *48*, 3842.
[19] K. Kim, J. Han, S. Maruyama, M. Balaban, I. Jeon, *Sol. RRL* **2021**, *5*, 2000783.
[20] T. Li, Y. Wang, W. Zhu, Q. Dang, Y. Zhang, Y. Li, X. Deng, *J. Mater. Chem. A* **2022**, *10*, 14441.
[21] Y. T. Yang, F. Hu, T. Y. Teng, C. H. Chen, J. Chen, N. Nizamani, K. L. Wang, Y. Xia, L. Huang, Z. K. Wang, *Angew. Chem.* **2024**, 202415681.
[22] H. Zhu, A. Liu, H. Kim, J. Hong, J. Y. Go, Y. Y. Noh, *Chem. Mater.* **2021**, *33*, 1174.
[23] Q. Liu, Y. Sun, M. Sun, Z. Fang, L. Li, D. Xie, C. Li, L. Ding, *J. Mater. Chem. C* **2019**, *7*, 5353.
[24] H. Min, J. Chang, Y. Tong, J. Wang, F. Zhang, Z. Feng, X. Bi, N. Chen, Z. Kuang, S. Wang, L. Yuan, H. Shi, N. Zhao, D. Qian, S. Xu, L. Zhu, N. Wang, W. Huang, J. Wang, *Nat. Photonics* **2023**, *17*, 755.
[25] C.-K. Liu, Q. Tai, N. Wang, G. Tang, H. L. Loi, F. Yan, *Adv. Sci.* **2019**, *6*, 1900751.
[26] F. Cao, W. Tian, M. Wang, M. Wang, L. Li, *InfoMat* **2020**, *2*, 577.
[27] F. Liu, K. Liu, S. Rafique, Z. Xu, W. Niu, X. Li, Y. Wang, L. Deng, J. Wang, X. Yue, T. Li, J. Wang, P. Ayala, C. Cong, Y. Qin, A. Yu, N. Chi, Y. Zhan, *Adv. Sci.* **2023**, *10*, 2205879.
[28] Z. Zhang, W. Zhai, G. Li, W. Zheng, X. Li, L. Huang, L. Chen, L. Lin, G. Yuan, Z. Yan, J. M. Liu, *ACS Appl. Mater. Interfaces* **2024**, *16*, 12773.
[29] L. Zhu, X. Cheng, A. Wang, Y. Shan, X. Cao, B. Cao, *Appl. Phys. Lett.* **2023**, *123*, 212105.
[30] D. Liu, K. Zhang, F. Liu, Y. Yin, X. Feng, C. Miao, M. Chen, X. Zhuang, X. Hao, Z. Yang, *Adv. Mater. Interfaces* **2021**, *8*, 2101339.
[31] E. Jokar, L. Cai, J. Han, E. John, C. Nacpil, I. Jeon, *Chem. Mater.* **2023**, *35*, 3404.
[32] Z. Lin, R. Huang, W. Zhang, Y. Zhang, J. Song, H. Li, D. Hou, Y. Guo, C. Song, N. Wan, P. K. Chu, *Adv. Funct. Mater.* **2018**, *28*, 1805214.
[33] S. Covella, V. Armenise, M. O. U. Rehman, E. Aktas, F. Fracassi, F. Palumbo, S. Colella, A. Abate, A. Listorti, *ACS Appl. Mater. Interfaces* **2024**, *16*, 49392.
[34] A. Perrotta, S. Covella, F. Russo, F. Palumbo, A. Milella, V. Armenise, F. Fracassi, A. Rizzo, S. Colella, W. Kaiser, A. A. Alothman, E. Mosconi, F. De Angelis, A. Listorti, *Sol. RRL* **2023**, *7*, 2300345.
[35] Z. Lin, H. Li, R. Huang, Y. Zhang, J. Song, H. Li, Y. Guo, C. Song, J. Robertson, *ACS Appl. Mater. Interfaces* **2017**, *9*, 22725.
[36] K. H. Lin, S. C. Liou, W. L. Chen, C. L. Wu, G. R. Lin, Y. M. Chang, *Opt. Express* **2013**, *21*, 23416.
[37] J. M. Heo, H. Cho, S. C. Lee, M. H. Park, J. S. Kim, H. Kim, J. Park, Y. H. Kim, H. J. Yun, E. Yoon, D. H. Kim, S. Ahn, S. J. Kwon, C. Y. Park, T. W. Lee, *ACS Energy Lett.* **2022**, *7*, 2807.
[38] B. Jiao, Y. Ye, L. Tan, Y. Liu, N. Ren, M. Li, J. Zhou, H. Li, Y. Chen, X. Li, C. Yi, *Adv. Mater.* **2024**, *36*, 2313673.
[39] W. Feng, Y. Tan, M. Yang, Y. Jiang, B. X. Lei, L. Wang, W. Q. Wu, *Chem* **2022**, *8*, 351.
[40] B. Liu, H. Chen, J. Cao, X. Chen, J. Xie, Y. Shu, F. Yan, W. Huang, T. Qin, *Adv. Funct. Mater.* **2023**, *34*, 2310828.
[41] Y. Xu, X. Guo, Z. Lin, Q. Wang, J. Su, J. Zhang, Y. Hao, K. Yang, J. Chang, *Angew. Chem., Int. Ed.* **2023**, *135*, e202306229.
[42] M. Krishnaiah, S. Kim, A. Kumar, D. Mishra, S. G. Seo, S. H. Jin, *Adv. Mater.* **2022**, *17*, 2109673.
[43] X. Ma, Y. Xu, S. Li, T. W. Lo, B. Zhang, A. L. Rogach, D. Lei, *Nano Lett.* **2021**, *21*, 9195.
[44] W. Gao, X. Liu, H. Jin, W. Li, X. Wang, R. Huang, G. Xing, H. Dong, Y. Zhou, Z. Wu, C. Ran, *ACS Energy Lett.* **2024**, *9*, 5045.
[45] D. Liu, Y.-X. Yin, F.-J. Liu, C.-C. Miao, X.-M. Zhuang, Z.-Y. Pang, M.-S. Xu, M. Chen, Z.-X. Yang, *Rare Met.* **2022**, *41*, 1753.

Supporting Information

Plasma-Enhanced Grain Growth and Non-Radiative Recombination Mitigation in $CsSnBr_3$ Perovskite Films for High-Performance, Lead-Free Photodetectors

Zewen Lin,† Zhenxu Lin,† Haixia Wu,† Rui Huang, Jie Song, Kaitao Chen, Li Xia, Yi Zhang, Huihong Lin, Hongliang Li, Dejian Hou, Yanqing Guo, and Paul K. Chu**

† These authors contributed equally to this work.

Dr. Z. Lin, Dr. Z. Lin, H. Wu, Prof. R. Huang, J. Song, K. Chen, L. Xia, Y. Zhang, Prof. H. Lin, H. Li, Prof. D. Hou, Prof. Y. Guo,
School of Materials Science and Engineering
Hanshan Normal University
Chaozhou, Guangdong 521041, P. R. China
E-mail: rhuang@hstc.edu.cn (R. Huang)

Prof. P. K. Chu
Department of Physics, Department of Materials Science and Engineering, and Department of Biomedical Engineering
City University of Hong Kong
Tat Chee Avenue, Kowloon, Hong Kong, China
E-mail: paul.chu@cityu.edu.hk (P. K. Chu)

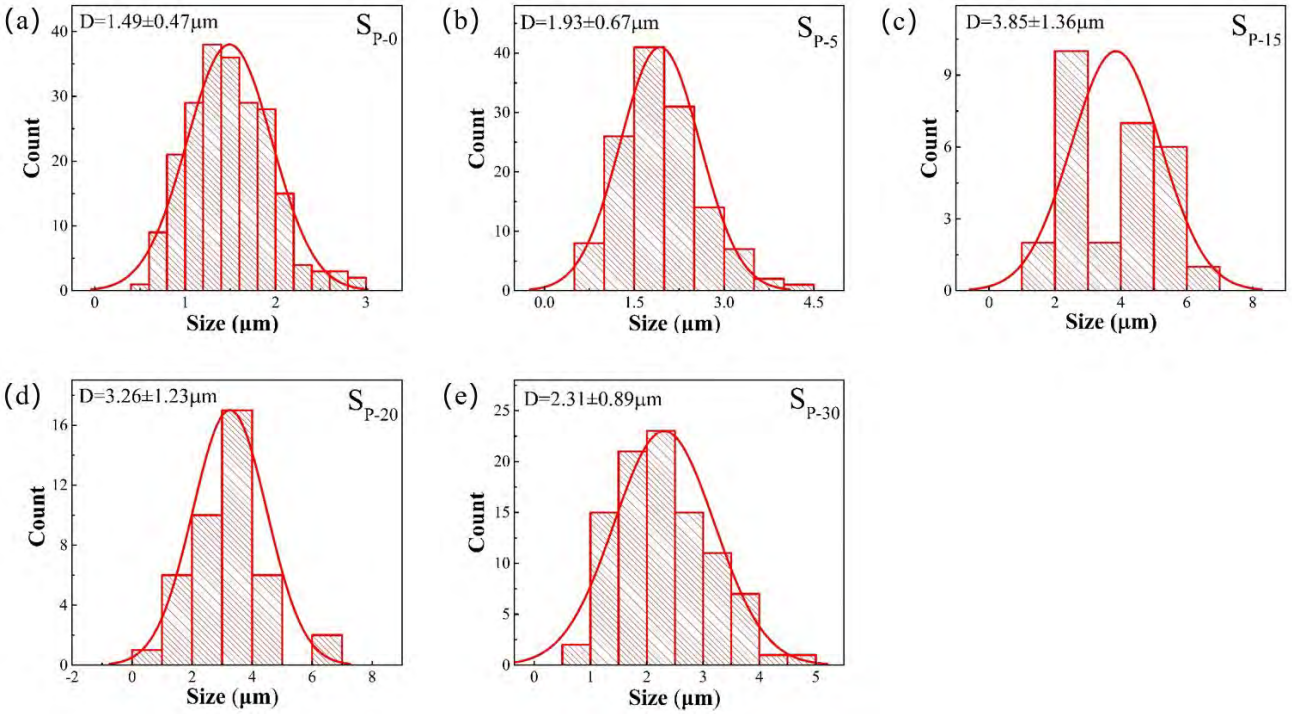

Figure S1. Diameter statistics of grains in $CsSnBr_3$ films deposited using different RF power settings: (a) No RF power, (b) 5 W, (c) 10 W, (d) 20 W, and (e) 30 W.

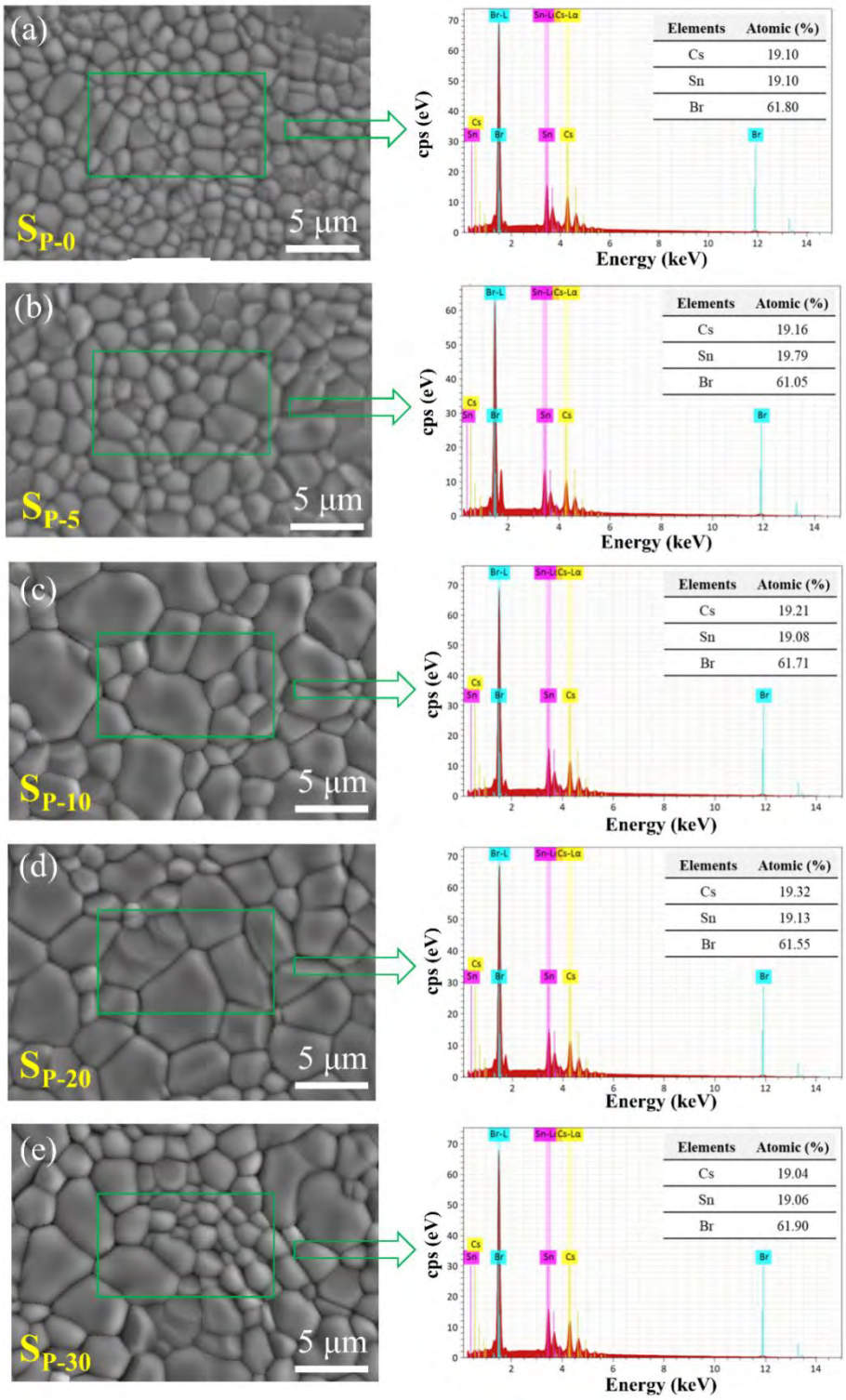

Figure S2. SEM images and EDS spectra of $CsSnBr_3$ films deposited using different RF power settings: (a) No RF power, (b) 5 W, (c) 10 W, (d) 20 W, and (e) 30 W.

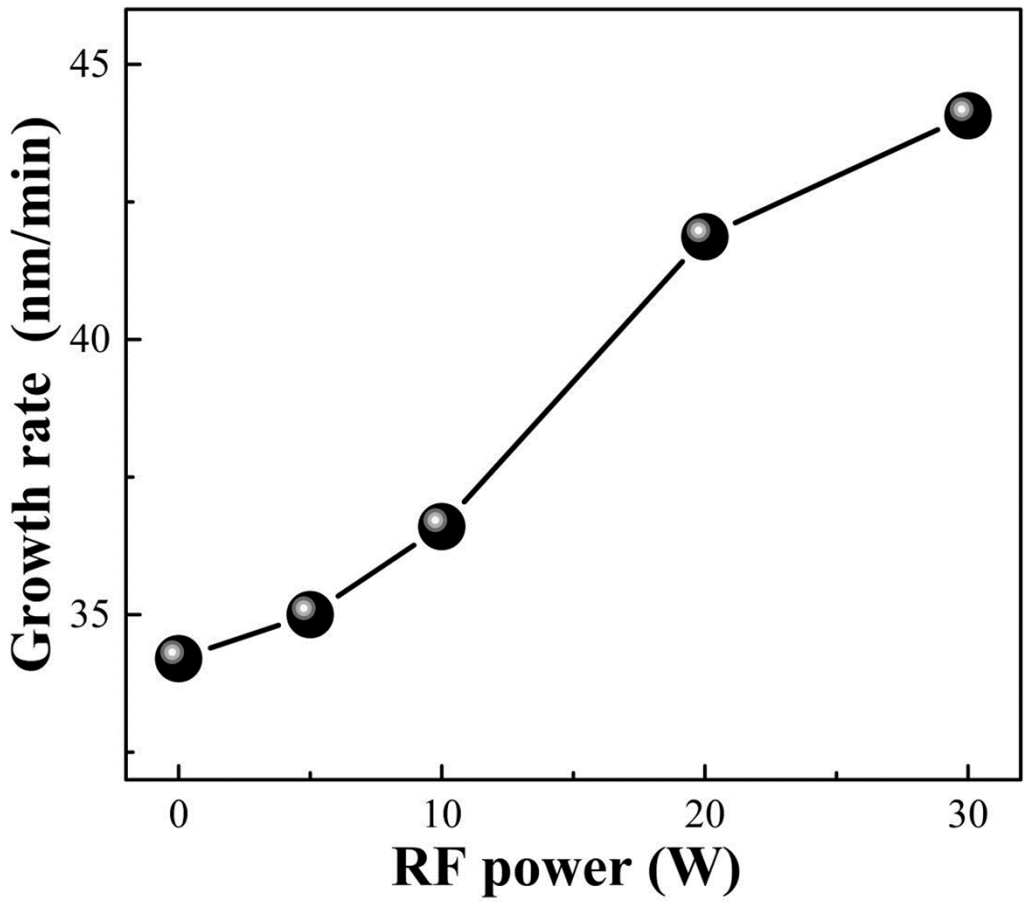

Figure S3. Deposition rates of $CsSnBr_3$ films as a function of RF power. The film deposition rate is defined as the thickness of the film divided by the growth time.

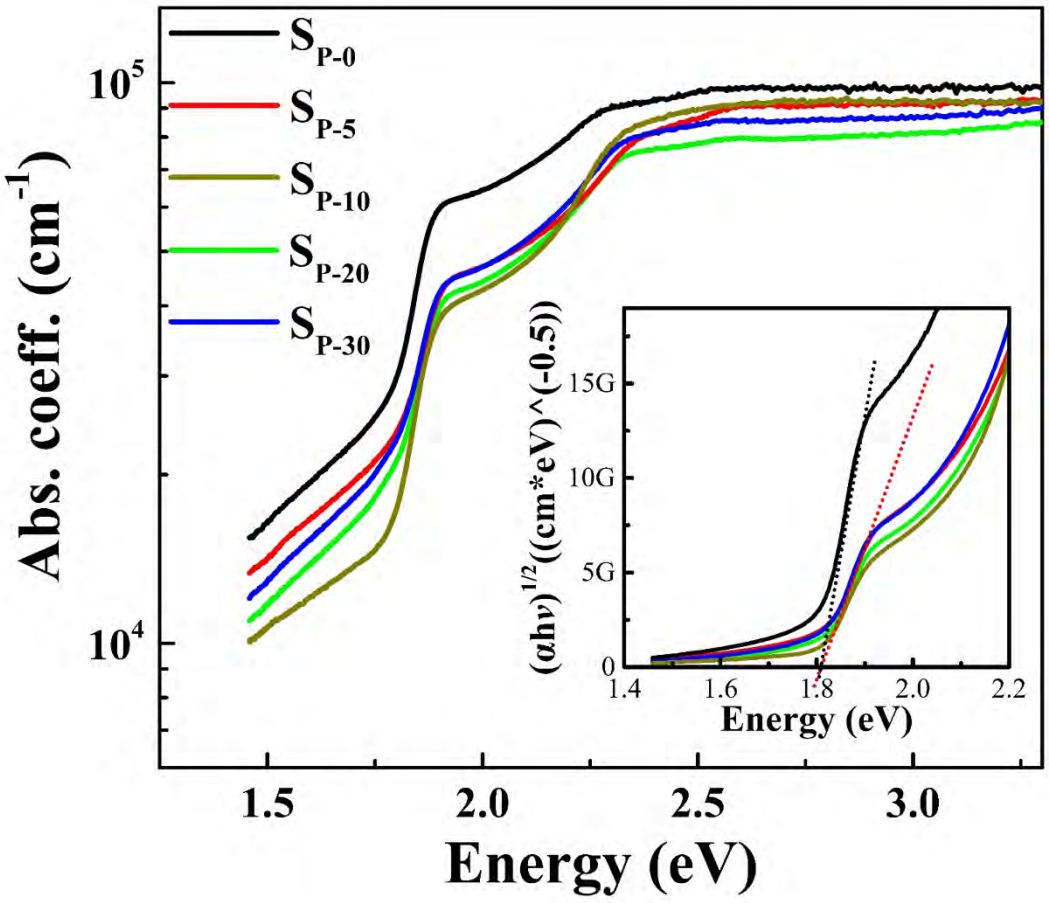

Figure S4. Optical absorption spectra of $CsSnBr_3$ films prepared using various RF power levels with the inset showing the Tauc plots of the $CsSnBr_3$ films derived from the absorption spectra.

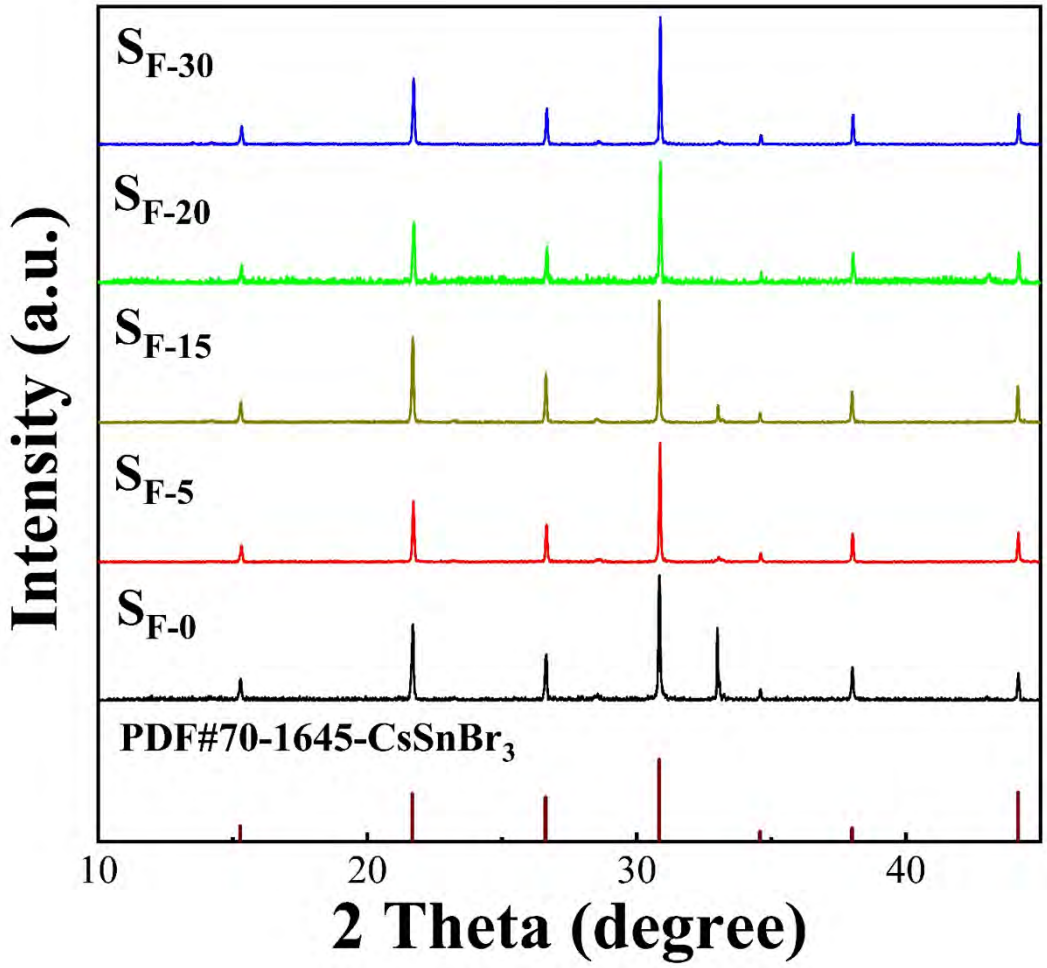

Figure S5. XRD patterns of $CsSnBr_3$ films prepared with different NH_3 flow rates.

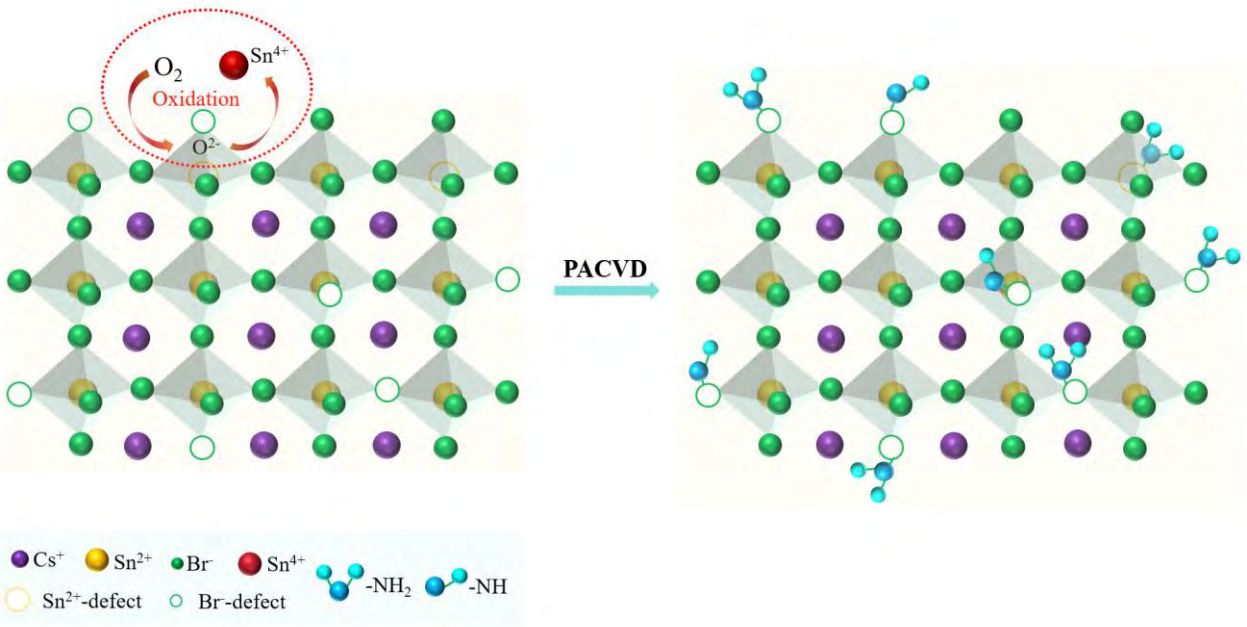

Figure S6. Schematic illustration of antioxidation and defect passivation of $CsSnBr_3$ films by PACVD with NH_3 plasma.

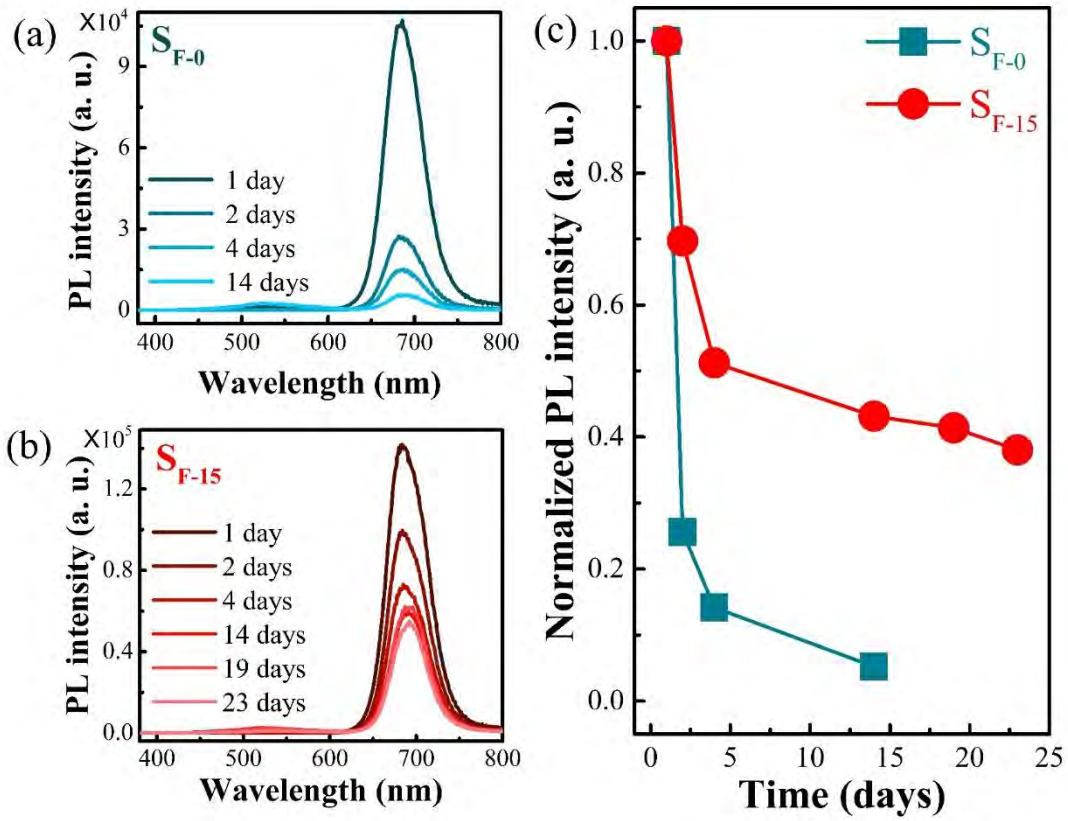

Figure S7. PL spectra of the $CsSnBr_3$ films prepared without NH_3 flow (a) and at an NH_3 flow rate of 15 sccm (b) at different time intervals under ambient conditions. (c) PL intensity as a function of time for both samples under ambient conditions.

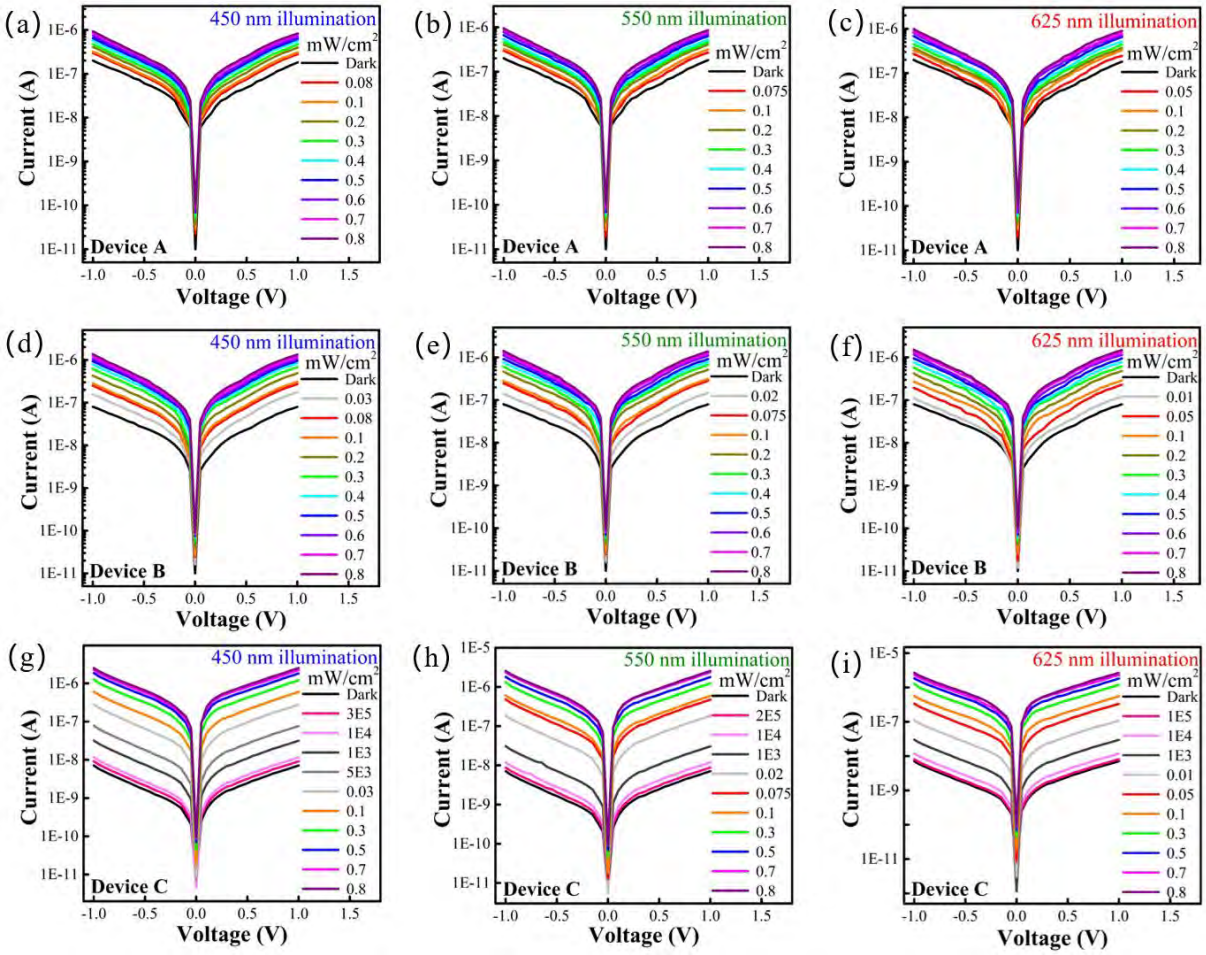

Figure S8. Logarithmic I–V curves of photodetectors based on $CsSnBr_3$ films grown under different conditions: (a-c) Device A, prepared without RF power, measured under 450 nm, 550 nm, and 625 nm illumination, respectively, with incident light power densities ranging from 0 to 0.8 mW cm^{-2}; (d-f) Device B, grown with Ar RF power of 10 W, measured under 450 nm, 550 nm, and 625 nm illumination, respectively, with incident light power densities from 0 to 0.8 mW cm^{-2}; (g-i) Device C, prepared with an NH_3 flow rate of 15 sccm and RF power of 10 W, measured under 450 nm, 550 nm, and 625 nm illumination, respectively, with incident light power densities ranging from 0 to 0.8 mW cm^{-2}.

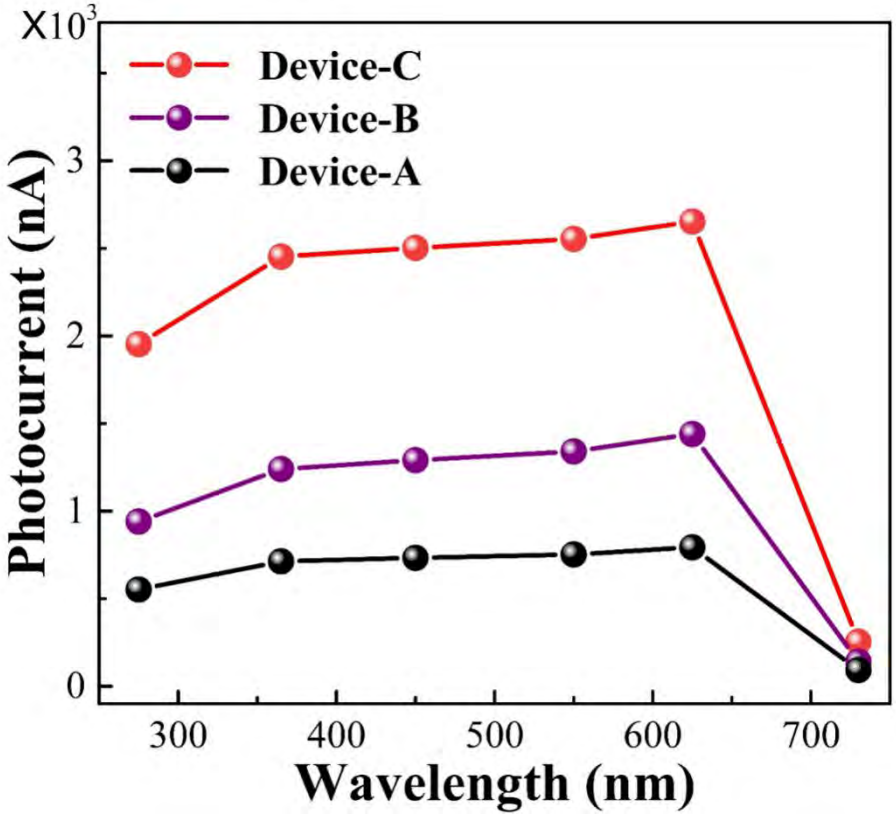

Figure S9. Photocurrents of device A, device B, and device C at different wavelengths with a laser intensity of 0.8 mW cm^{-2}.

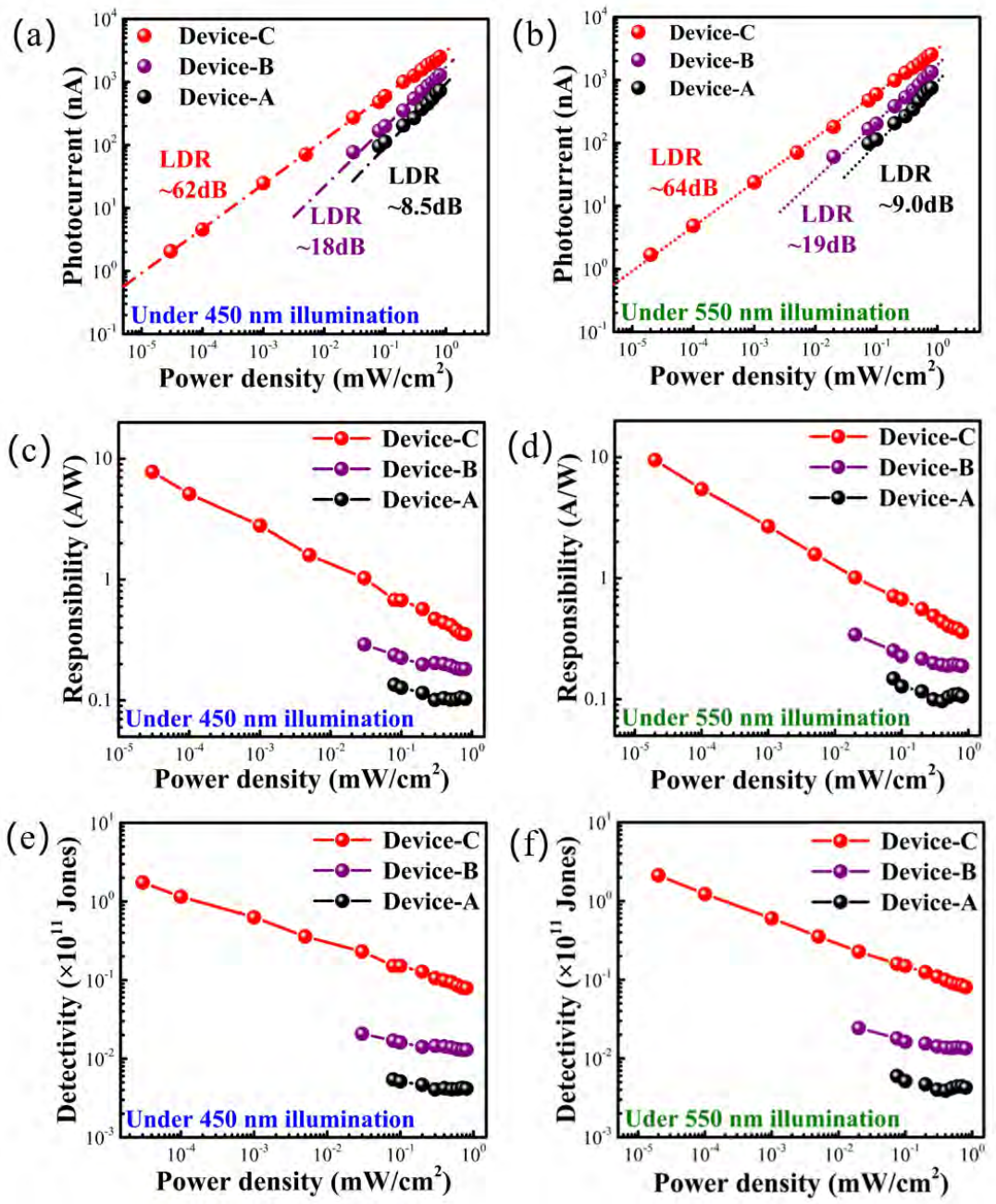

Figure S10. (a, b) Photocurrent dependence on illumination power densities; (c, d) Responsivity (R); and (e, f) Specific detectivity (D*) for devices A, B, and C under illumination with 450 nm and 550 nm lasers, respectively, at an intensity of 0.8 mW cm^{-2}.

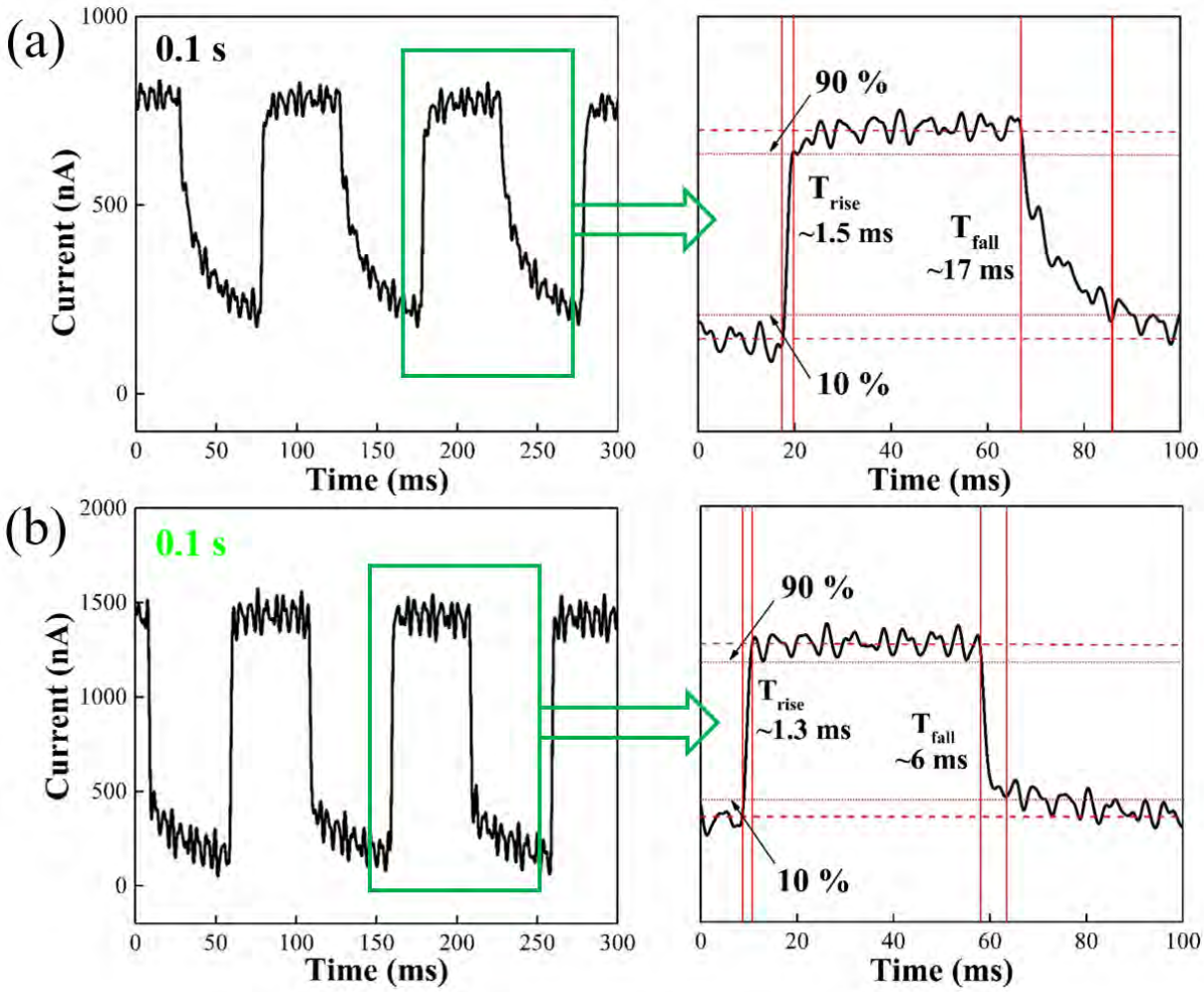

Figure S11. Time-response curves, including rise and decay times, of (a) Device A and (b) Device B under 625 nm laser illumination.

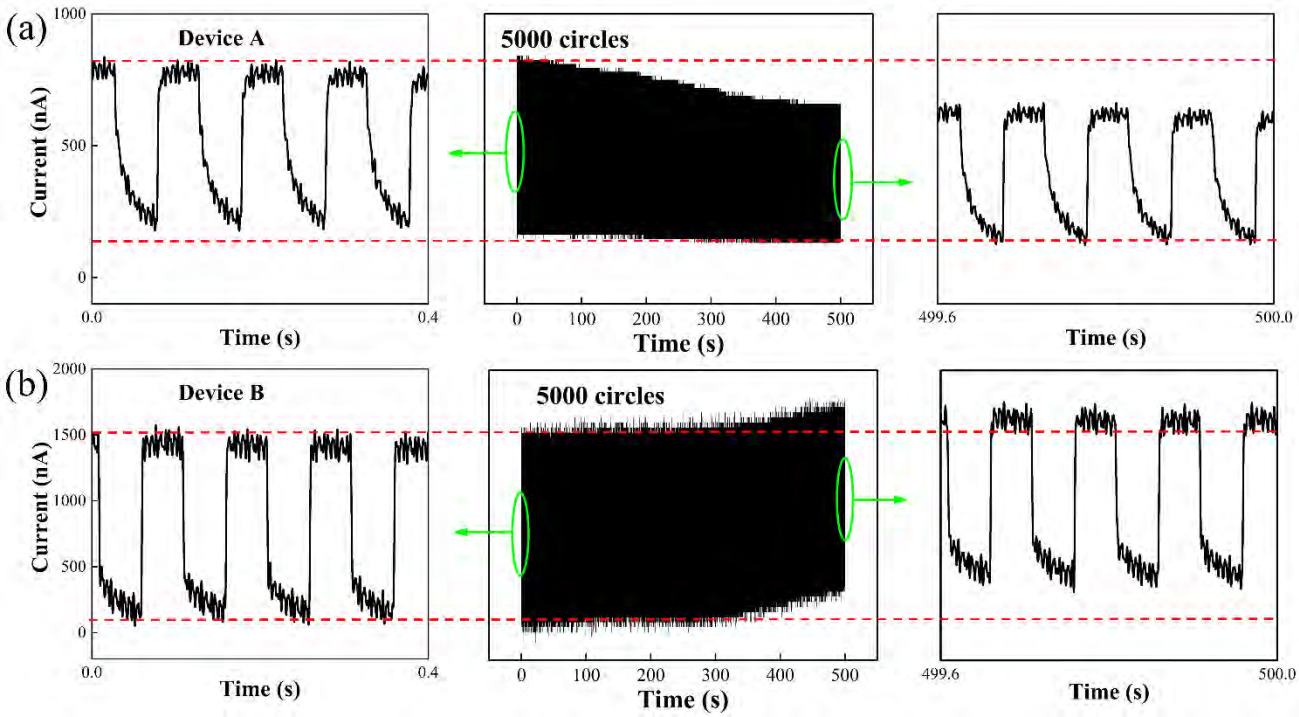

Figure S12. Current-time (I–t) curves of (a) Device A and (b) Device B under a bias voltage of 1 V and illuminated by 0.8 mW cm^{-2}

Table S1. Summary of properties of photodetectors fabricated with organic or inorganic lead-free halide perovskite materials.

Absorbers	Detection Style	D* (Jones)	R (A W-1)	T_{rise}/T_{fall}	Ref.
$MASnI_3$ NW arrays	Visible Detection	8.80×10^{10}	0.47	1500 ms/400 ms	1
$FASnI_3$ film	VIS-NIR Detection	-	2.90	-	2
Cs_2SnI_6 particles	UV–VIS–NIR Detection	5.95×10^{10}	6.25	23 ms/28ms	3
$TBASnCl_3$ QDs	UV Detection	1.67×10^{11}	0.0073	62.8 s/66.4 s	4
$CsSnI_3$/CNT composite	Visible Detection	-	0.01	-	5
$CsSnBr_3$ film	Visible Detection	5.8×10^{7}	9.2	5 ms/12 ms	6
$CsSnBr_3$ film	Visible Detection	1.22×10^{9}	4.89	3 ms/10 ms	7
$CsSnBr_3$ QDs	UV–VIS Detection	4.27×10^{11}	0.0623	50 ms/51 ms	8
$CsPb_xSn_{1-x}Br_3$ NWs	Visible Detection	2×10^{10}	0.011	4.25 ms/4.82 ms	9
$CsSnBr_3$ film	Visible Detection	2.5×10^{11}	11.3	1.0 ms/3.3 ms	This work

"–": not available

References

[1] A. Waleed, M. M. Tavakoli, L. Gu, Z. Wang, D. Zhang, A. Manikandan, Q. Zhang, R. Zhang, Y. L. Chueh, Z. Fan, *Nano Lett.* **2017**, *17*, 523.

[2] Z. Zhang, W. Zhai, G. Li, W. Zheng, X. Li, L. Huang, L. Chen, L. Lin, G. Yuan, Z. Yan, J. M. Liu, *ACS Appl. Mater. Interfaces* **2024**, *16*, 12773.

[3] M. Krishnaiah, S. Kim, A. Kumar, D. Mishra, S. G. Seo, S. H. Jin, *Adv. Mater.* **2022**, *17*, 2109673.

[4] Z. Zhang, S. Yang, J. Hu, H. Peng, H. Li, P. Tang, Y. Jiang, L. Tang, B. Zou, *Nanoscale* **2022**, *14*, 4170.

[5] A. H. Howlader, F. Li, R. Zheng, *Emergent Mater.* **2022**, *5*, 1925.

[6] D. Liu, K. Zhang, F. Liu, Y. Yin, X. Feng, C. Miao, M. Chen, X. Zhuang, X. Hao, Z. Yang, *Adv. Mater. Interfaces* **2021**, *8*, 2101339.

[7] D. Liu, Y. X. Yin, F. J. Liu, C. C. Miao, X. M. Zhuang, Z. Y. Pang, M. S. Xu, M. Chen, Z. X. Yang, *Rare Metals* **2022**, *41*, 1753.

[8] X. Ma, Y. Xu, S. Li, T. W. Lo, B. Zhang, A. L. Rogach, D. Lei, *Nano Lett.* **2021**, *21*, 9195.

[9] X. Tang, H. Zhou, X. Pan, R. Liu, D. Wu, H. Wang, *ACS Appl. Mater. Interfaces* **2020**, *12*, 4843.